

In Situ Observation of Alignment Templating by Seed Crystals in Highly Anisotropic Polymer Transistors

Nils E. Persson,[†] Sebastian Engmann,^{‡,§} Lee J. Richter,[†] and Dean M. DeLongchamp^{*,†}

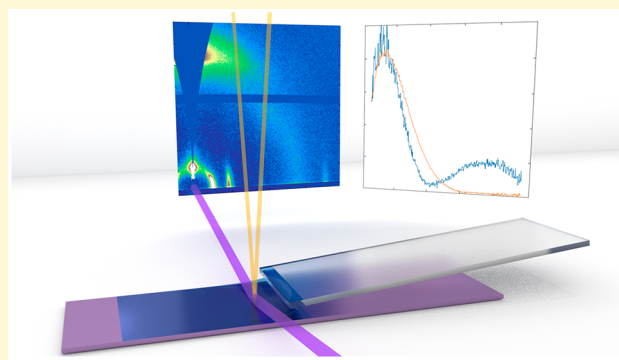
[†]Materials Science and Engineering Division, National Institute of Standards and Technology, 100 Bureau Drive, Gaithersburg, Maryland 20899, United States

[‡]Theiss Research, La Jolla, California 92037, United States

[§]Nanoscale Device Characterization Division, National Institute of Standards and Technology, 100 Bureau Drive, Gaithersburg, Maryland 20899, United States

S Supporting Information

ABSTRACT: Due to the highly directional nature of transport in polymer-based organic field-effect transistors (OFETs), alignment of the polymer backbone can significantly affect device performance. While many methods of alignment have been detailed, the mechanism of alignment is rarely revealed—especially in cases of flow-induced alignment. Polymer aggregates are often observed in highly aligned systems, but their role is similarly unclear. Here, we present a comprehensive characterization of blade-coated P(NDI2OD-T2) (N2200) for OFET applications, including a rigorous, multimodal characterization of its in-plane alignment. Film thickness follows the expected power-law dependence on coating speed, while bulk polymer backbone orientation transitions from perpendicular to parallel to the coating direction as speed is increased. Charge carrier mobility $>2 \text{ cm}^2/(\text{V s})$ is achieved parallel to the coating direction for aligned N2200 coated at 5 mm/s and is found to be strongly correlated with the in-plane alignment of the fibrillar morphology at the film's surface, characterized with atomic force microscopy and near-edge X-ray absorption. We develop a model of N2200 crystal anisotropy through rotational scans of grazing incidence wide-angle X-ray scattering (GIWAXS) and use it to analyze simultaneous *in situ* GIWAXS and UV–vis reflectance data from polymer solutions coated at 5 mm/s. A small population of crystals align early in the drying process, but bulk alignment occurs very late in the drying process, likely mediated by a lyotropic liquid crystal phase transition templated by the aligned crystals. Our characterization also suggests that the majority of material in N2200 thin films is noncrystalline at these conditions.



Solution-processed polymer semiconductors have made remarkable progress toward commercial viability in recent years, with applications being demonstrated in displays,¹ sensors,^{2,3} and logical circuits.⁴ The promise of these materials lies in their combination of chemical tunability, mechanical flexibility, and their amenability to large-area coating techniques used in roll-to-roll processing.⁵ While solution processing offers the advantages of being additive, low-temperature, and scalable, it is difficult to control thin film structural organization during film drying due to the complex interplay of kinetic and thermodynamic factors.^{6,7} Variations in coating process parameters can lead to a wide diversity of structures, each with unique electrical properties. The extreme anisotropy of the local electronic structure of semiconducting polymers, conjugation along the backbone, possible π orbital overlap between conjugated planes, and negligible conduction through solubilizing side chains, suggests that electronic properties will be strongly modulated in films with overall alignment. Roll-to-roll coating techniques are generally unidirectional, favoring orientationally aligned structures with commensurate charge

transport anisotropy.^{8,9} However, structural alignment is not by any means guaranteed, and the mechanism of alignment during drying is poorly understood. The goal of this study is to better characterize the evolution of structural alignment in a solution-processed *n*-type semiconducting polymer, poly{[*N,N'*-bis(2-octyldodecyl)-1,4,5,8-naphthalenedicarboximide-2,6-diyl]-*alt*-5,5'-(2,2'-bithiophene)} (P(NDI2OD-T2) or Polyera ActivInk N2200), through a combination of *ex situ* and *in situ* methods.

Structural order can be promoted through the use of poor or marginal solvents that favor polymer aggregation, obviating the need for slower directional crystallization techniques or post-treatments such as strain alignment.^{10–12} Recent investigations into the solution processing of N2200 have demonstrated its propensity to aggregate in marginal and poor solvents.^{13,14} The polymer aggregates present as high-aspect-ratio fibrillar structures when characterized via atomic force microscopy

Received: March 4, 2019

Revised: May 11, 2019

Published: May 13, 2019

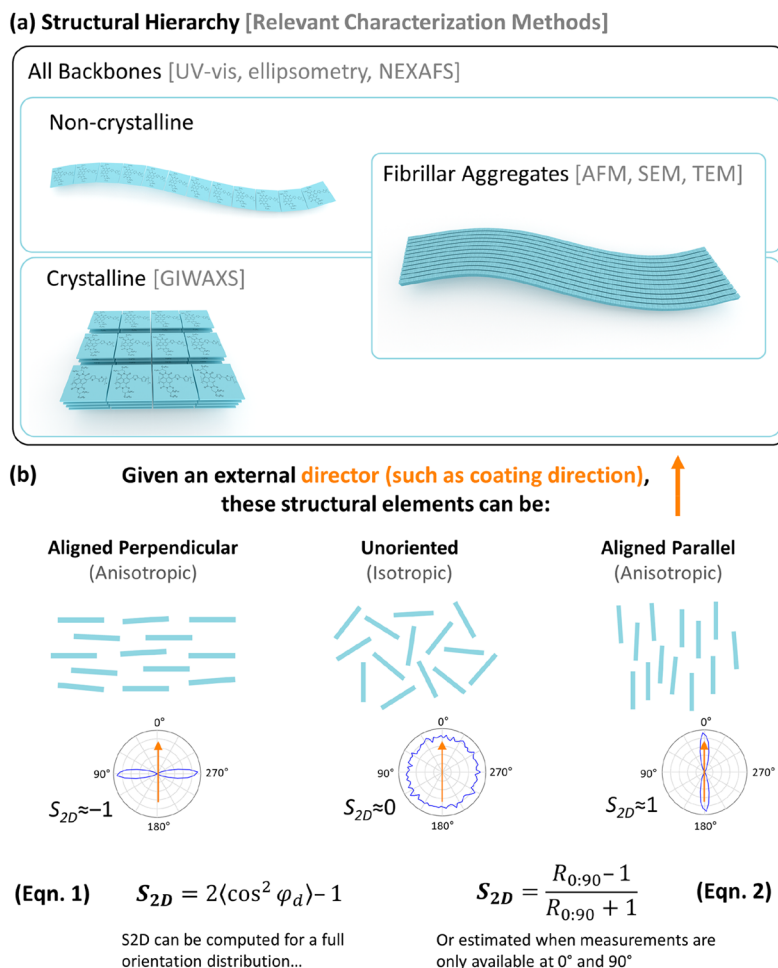


Figure 1. Guide to oriented structural elements of polymer thin films and the language used to describe their organization.

(AFM) after thin film deposition. When wire-bar-coated or brush-coated, these fibrillar thin films become uniaxially oriented and demonstrate device-scale mobility anisotropy.^{15,16} Blade coating is similar to these techniques, with greater relevance to roll-to-roll processes such as slot die coating, while presenting fewer nonidealities in the coating surface such as grooves or brush hairs.^{17,18} Blade coating is an ideal process in which to study the development of polymer alignment because it can be instrumented for both *in situ* optical and X-ray-based characterization. Specific questions to be answered include the following: when and how during blade coating is long-range alignment achieved, what role do polymer aggregates play, and how does polymer alignment vary spatially?

Oriented assembly of polymer aggregates, or fibrils, during blade coating depends upon solvent evaporation, fluid convection, and confinement and interfacial effects.¹⁹ Blade coating has previously been applied to other semiconducting polymers, such as poly(3-hexylthiophene) (P3HT) and diketopyrrolopyrrole-thienothiophene-based copolymers (P-(DPP-X)). Chu et al. found that blade-coated P3HT fibrils tended to orient with the fibril long axis parallel to the coating direction, yielding thin film transistors with maximum mobility *perpendicular* to the coating direction.²⁰ This was rationalized by the fact that P3HT fibrils have the chain backbone perpendicular to the long axis of the fibril. The air interface had longer fibrils and stronger alignment than the buried SiO₂ interface, suggesting that alignment was driven by organization at the air

interface.²¹ P(DPP2T-TT) displayed similar behavior when blade-coated at 0.5 mm/s in the evaporative regime: fibrils aligned strongly in the coating direction at the air interface, but were unoriented or even aligned perpendicular to the coating direction in the bulk.²² It was suggested that elongational flow from solvent evaporation produced torques that aligned the fibrils. It was also observed that mobility at the top surface was highest in the coating direction, because polymer backbones were parallel to the long axis of the fibrils. Shaw et al. built on these observations by identifying three distinct regimes of crystallization behavior for blade-coated P(DPP3T) using *in situ* grazing incidence wide-angle X-ray scattering (GIWAXS) measurements, revealing a delicate interplay between interface nucleation, solution shear, and drying speed.²³

N2200 displays unique textural features that separate it from most semiconducting polymers, making it an interesting candidate for the study of polymer alignment during blade coating. A recent investigation by Trefz et al. demonstrated that blade-coated thin films of N2200 contained fibrils with the polymer backbone parallel to the fibril backbone, with a face-on out-of-plane orientation.²⁴ This orientation places the *a*- and *c*-axes of the crystalline phase in the plane of the substrate, which potentially allows for the determination of in-plane crystal orientation through *in situ* GIWAXS measurements during blade coating. Trefz also found indirect evidence that polymer alignment was mediated by a liquid crystalline phase; studies of PBTTT (poly(2,5-bis(3-alkylthiophen-2-yl)thieno[3,2-b]-

thiophene)), PCDTPT ((poly[4-(4,4-dihexadecyl-4*H*-cyclopenta[1,2-*b*:5,4-*b'*]dithiophen-2-yl)-*alt*-[1,2,5]thiadiazolo[3,4-*c*]pyridine])), and CDTBTZ ((poly-[2,6-(4,4-bis-alkyl-4*H*-cyclopenta[2,1-*b*;3,4-*b'*]-dithiophene)-*alt*-4,7-(2,1,3-benzothiadiazole)])) have also identified liquid crystallinity as a driving force for alignment, potentially templated by oriented seed crystals.^{17,25} To definitively characterize the interaction between crystals and liquid crystals during film drying, we performed simultaneous *in situ* GIWAXS and optical measurements during blade coating of N2200 from toluene. These *in situ* measurements are supported through detailed structural analysis and transistor measurements. We identify a remarkable range of attainable structures with commensurate variations in charge transport, as well as the mechanism of structural alignment for the high-performance, high-alignment case.

■ BACKGROUND AND THEORY

At its core, this is a study of oriented objects: polymer backbones, polymer crystals, and aggregated polymer fibrils. Each of these objects have well-defined 3-dimensional orientations that are probed by different structural characterization techniques. The language surrounding oriented objects can be somewhat ambiguous, with “orientation”, “orientational order”, “anisotropy”, and “alignment” sometimes being used interchangeably. The precise usage of these terms is crucial to understanding the results presented here as well as the results of the numerous other studies on oriented and aligned semiconducting polymers. For this reason, we are including in the main text (Figure 1) a guide to the language and metrics used to describe the oriented structural elements frequently characterized in semiconducting polymers.

Here, the most granular level of orientation we will consider is that of a single polymer repeat unit. We represent repeat units as rigid plates, an approach taken by other authors in the coarse-graining of molecular dynamics simulations and frequently used in illustrations of semiconducting polymers.²⁶ This representation ignores the flexibility of the side chains and possible backbone torsion within the repeat unit but is very useful in schematic illustrations. The orientation of repeat units (and thus the local *polymer backbone*) is generally probed by the interaction of their transition dipole moment tensor with an incident optical beam, measured by spectroscopy techniques such as UV–vis absorption, spectroscopic ellipsometry (SE), and near-edge X-ray absorption fine structure (NEXAFS).²⁷ Through some analysis, these techniques can yield an ensemble average of polymer backbone orientation, regardless of the backbones' involvement in crystals, aggregates, or fibrils. In other words, these techniques measure all the material in the thin film within the beam footprint. In favorable cases, transition energies can be correlated to local order (conjugation length), and one can independently characterize regions of high and low order.²⁸

GIWAXS (and other scattering techniques) measures objects arranged into periodic lattices, usually referred to as *crystals*. A crystal's orientation is defined by its lattice vectors; GIWAXS yields an integration (sum) of the scattering from lattices of crystalline material within the X-ray beam footprint. Scattering can only be measured for lattice vectors that obey the Bragg condition. Local regions of polymer backbones can be a part of crystals; this does not mean that the entire backbone is crystalline. Thus, GIWAXS only measures a subset of the total backbone population.²⁹ The size of crystalline regions can vary,

and in materials with substantial paracrystallinity (such as semiconducting polymers), their size is more accurately described by a crystalline coherence length, rather than grain size.

Finally, *fibrils* [also referred to as (nano)fibers or wires] are a structural element observed almost exclusively by imaging techniques such as AFM, scanning electron microscopy (SEM), and transmission electron microscopy (TEM).^{30,31} They manifest as high-aspect-ratio objects in the image, with contrast produced by their elevated height or differing mechanical properties (in AFM height and phase channels, respectively) or by their electron density in electron microscopy. A fibril may be composed of up to thousands of polymer backbones and is thus a form of polymer aggregate. The orientation of the backbones need not be the same as the orientation of the fibril's long axis. In some fibril-forming semiconducting polymers (e.g., P3HT), the backbone is oriented perpendicular to the fibril long axis. This is sometimes referred to as a “kebab-style” fibril.^{32,33} In Figure 1a, we depict the polymer backbone parallel to the fibril long axis, because it has been shown that this is the case for N2200. This configuration is referred to as a “shish-style” fibril. Fibrils are not necessarily comprehensively crystalline, even though fibrils of semiconducting polymers are generally quite stiff (have a high persistence length).²¹ The populations of crystalline and fibrillar material likely strongly overlap, but there can be crystalline material not involved in fibrils and regions of fibrils that are not crystalline.³⁴

These three structural elements—backbones, crystals, and fibrils—are members of populations that collectively have orientation distribution functions, or ODFs. Local, nonscalar material properties, such as charge carrier mobility, can also have orientation distributions. For orientation distributions that are centrosymmetric, as usually encountered for liquid crystals and polymer fibrils, the first nonvanishing moment of the angle φ between an element and the director is quadratic. Two order parameters are often introduced: the Herman's S parameter, $\frac{1}{2}(3\cos^2\varphi - 1)$, appropriate for 3D systems such as nematic liquid crystals, and $S_{2D} = 2\langle\cos^2\varphi\rangle - 1$, commonly adopted for distributions confined to a 2D plane. The $\langle\Box\rangle$ brackets denote the average over the ODF of the identified population. As will be shown, the dominant features for N2200 (backbone director, crystal-*c*-axis, fibril long axis) are strongly confined to the surface plane, and thus, S_{2D} will be used to characterize their ODF throughout the Article. In this study, we fix the director to be the coating direction; in other use cases, the director could vary according to the local average orientation.³⁵ The squared term means that there is symmetry about the line between 90° and 270°. For example, φ_d of 45° and 135° (and 225° and 315°) will yield the same values of $\langle\cos^2\varphi_d\rangle$ and S_{2D} : +1/2 and 0, respectively. Also because of this, the distributions presented in this study are also forced to have 180° rotational symmetry—the full 360° plots are used to aid in visual interpretation.

As illustrated in Figure 1b, a population with no preferential orientation is referred to as “unoriented” or “isotropic” (i.e., having no directional dependence), and an isotropic 2D orientation distribution yields an S_{2D} of 0. Note, however, that a population uniformly oriented at 45° (and/or 135°, 225°, 315°) off of the director (a /- or X-shaped distribution) will also yield an $S_{2D} = 0$, following from the example above. In this sense, 45° is the “magic angle” of in-plane alignment measurements. Populations with higher alignment in any direction are said to be “anisotropic”; alignment parallel to the director will cause S_{2D} to

approach 1, while alignment perpendicular to the director will push S_{2D} closer to -1 . Through this Article, we will use S_{2D} and anisotropy interchangeably and reserve the term alignment for more general characterization of the ODF.

Linear dichroism techniques (UV-vis, ellipsometry, and NEXAFS) are limited to reconstructing the second-order dielectric tensor and thus can only provide information on the second moment of the ODF^{36,37} and as such directly provide S_{2D} . In these cases, the complete information on the measurement of $\langle \cos^2 \varphi \rangle$ is contained in the measurement of the ratio of the response at 0° and 90° ($R_{0:90}$) using eq 2 in Figure 1. A common example of $R_{0:90}$ is the “dichroic ratio” frequently used to characterize UV-vis anisotropy. However, as is clear from the preceding discussion, S_{2D} only gives direct insight into an overall alignment direction (perpendicular or parallel to the director) but does not uniquely define the ODF shape, i.e., whether the ODF is narrow or broad. Measurement of higher moments of the ODF are required to obtain this insight.³⁸ In some cases, the complete orientation distribution of a population is measurable by finely discretized real-space (AFM) or reciprocal-space (GIWAXS), measurements. Throughout this Article, we report S_{2D} either from eq 2 in Figure 1 or from numerical integration of the discrete distribution, as appropriate.

RESULTS AND DISCUSSION

Film Thickness and Backbone Orientation vs Coating Speed. The character of films fabricated using meniscus-guided coating methods such as blade coating depends significantly on coating speed. Two regimes are expected: a low-speed evaporative regime where film thickness decreases with increasing speed and a higher-speed Landau–Levich–Derjaguin (LLD) regime where film thickness increases with increasing speed. The specific dependence that is found in each regime and the crossover between regimes depends on the combination of solution characteristics and drying conditions.

We first characterized film thickness and in-plane polymer backbone orientation as a function of coating speed using spectroscopic ellipsometry (SE) measurements in Mueller Matrix mode with the scattering plane oriented at 0° , 45° , and 90° with respect to the coating direction. The SE data were fitted using a single-layer optical model for the N2200 thin film, meaning that the film was treated as a single slab with spatially homogeneous optical properties. While surface layers with orientations differing from the bulk have been previously observed in N2200, the additional model parameters introduced by adding more layers would likely result in overfitting, without providing definitive structural insight. The results from SE should thus be considered bulk or average measurements for the entire film.

The single-layer model was based on a biaxial, diagonal dielectric function, assuming nominal orthorhombic symmetry of the film, and thus neglects any “pretilt” in the film, consistent with the GIWAXS result below. The three distinct, causal dielectric functions ϵ_{xx} , ϵ_{yy} , and ϵ_{zz} were fitted to the SE data with z along the surface normal and x along the coating direction. Within a linear effective medium approximation (oriented gas model) and assuming the local dielectric function is dominated by a single transition oriented along the polymer chain backbone, the three components of the dielectric function provide a measurement of the projection of the backbone against the surface normal $\langle \cos^2 \theta \rangle$ and of the projection in the surface plane $\langle \cos^2 \varphi \rangle$. The alignment of the backbone has been hypothesized to correlate strongly with mobility and charge

transport anisotropy for semiconducting polymers.^{11,16,20} We consistently find that the imaginary part of the ϵ_{zz} component is small, indicating nearly comprehensive alignment of the polymer chains into the surface plane, $\langle \cos^2 \theta \rangle \approx 1$. From the ratio of the imaginary part of ϵ_{xx} and ϵ_{yy} we obtain S_{2D} , shown in Figure 2a. See the Supporting Information, Section S1, for

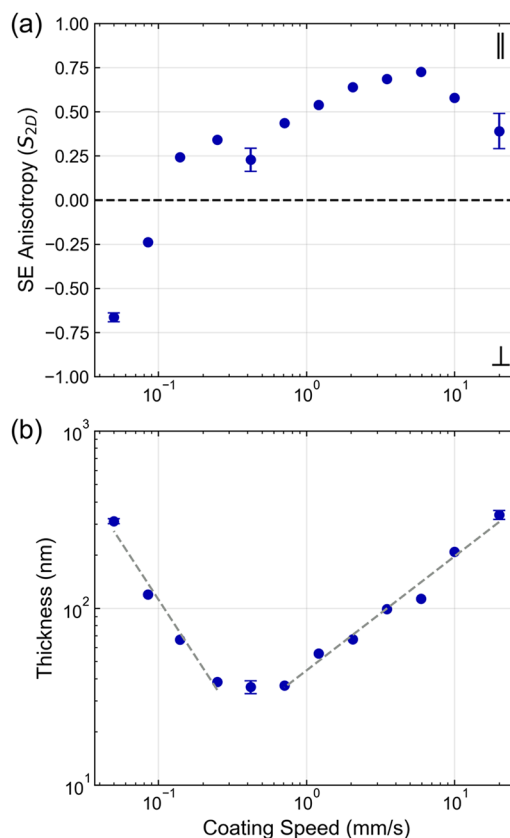


Figure 2. Backbone anisotropy (a) and film thickness (b) as measured by SE. Coating speed was varied from 0.05 to 20 mm/s on a log scale. Backbone anisotropy is reported as S_{2D} , calculated as described in the text. Dotted lines indicate power-law fits to the thickness data in the evaporative and Landau–Levich regimes. Representative error bars are shown on three points (0.05, 0.42, and 20 mm/s) as the standard deviation of ≥ 3 replicate measurements at different locations on the same film.

details of the model and fitting. S_{2D} derived from SE is equivalent to that obtained from ultraviolet–visible spectroscopy (UV-vis) measurements according to eq 2 in Figure 1.

Film thickness, obtained from the same SE model fit, is plotted in Figure 2b. The thickness of blade-coated films follows a power-law dependence upon coating speed, separated into two regimes.³⁹ In the low-speed evaporative regime, film drying is mass-transfer-limited at the free surface, and thickness decreases with coating speed, here with an exponent of ≈ -1.3 , according to a linear regression fit of the four points showing decreasing thickness with increasing coating speed. A minimum film thickness of ≈ 20 nm is reached at the transition point at ≈ 0.3 mm/s. Above this point is the LLD regime, in which thickness increases with speed with an exponent of ≈ 0.65 , obtained by a similar power-law fit, in agreement with theory.^{40,41}

There is no generally accepted or theoretical expectation for the dependence of backbone orientation on speed; indeed, N2200 is notable in how universally it orients across a wide

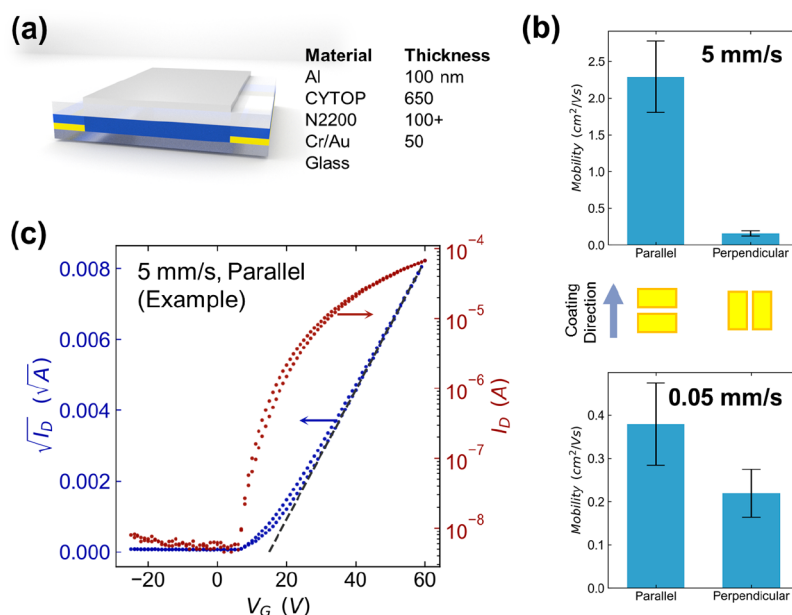


Figure 3. Organic field-effect transistor OFET fabrication and characterization. (a) Top-gate device architecture with materials used and their thickness. (b) Saturation regime electron mobility from transistor channels oriented parallel and perpendicular to the coating direction at 5 and 0.05 mm/s. Error bars indicate the standard deviation among ≥ 7 devices with channel lengths of 50 or 100 μm . (c) Example transfer curve from a channel parallel to the coat at 5 mm/s, overlaid with the saturation regime model fit used to extract mobility (solid blue line).

range of velocities.^{17,18} As seen in Figure 2a, S_{2D} ranges from ≈ -0.65 at 0.05 mm/s (polymer backbones aligned preferentially perpendicular to the coating direction) to ≈ 0.75 at 5.93 mm/s (aligned preferentially parallel to the coating direction). In other studies of unidirectionally coated N2200, backbone alignment parallel to the coating direction has been observed, but the perpendicular alignment we observe at low speed has not been previously reported. The flip to perpendicular alignment occurs deep in the evaporative regime, at film thicknesses >100 nm. Obtaining films at velocities below 0.05 mm/s was infeasible due to coater constraints as well as concerns over solvent evaporation from the droplet reservoir. Also of note, at velocities above ≈ 6 mm/s, backbones became more isotropic (S_{2D} decreases) as film thickness continued to increase. These phenomena will be discussed in detail in a later section once all structural data have been introduced.

Charge Transport Anisotropy. Since polymer backbone alignment has been shown in previous studies of N2200 to maximize the absolute magnitude of charge transport as well as its anisotropy, we chose to fabricate thin film transistor (TFT) devices at the coating speeds yielding the highest magnitudes of S_{2D} : 0.05 and 5 mm/s (chosen instead of 5.93 mm/s for ease of discussion). Early studies of N2200 found its performance to be limited to <0.1 cm²/(V s) in a bottom-gate architecture; our initial exploration of bottom-gate devices confirmed this. We chose to use a top-gate architecture to achieve optimal application-relevant performance, in line with recent studies on the material. Our bottom-contact, top-gate device architecture is illustrated in Figure 3a, consisting of a glass substrate, 50 nm Au source/drain electrodes with a Cr adhesion layer, the blade-coated active layer of N2200, a spin-coated Bellex CYTOP-M (CYTOP) gate dielectric, and an Al gate electrode. Each substrate was patterned with an 8×8 grid of such device channels, with alternating columns of electrodes oriented parallel and perpendicular to the coating direction to extract charge transport anisotropy from a single coating. We note here that N2200 is an *n*-type material, meaning that the

device's "on" state occurs with positive V_{DS} and positive V_{GS} .⁴² The positive gate bias lowers the energy levels of the material near the CYTOP/N2200 interface, allowing for electron injection into the lowest unoccupied molecular orbital (LUMO) of N2200. As illustrated in Figure 3c, transfer curves were mostly ideal with small hysteresis, V_T between ≈ 10 and 20 V, and free of strong curvature indicative of gate-bias-dependent mobility.⁴³ Transfer curves for the 0.05 mm/s devices, as well as output curves for both conditions, can be found in Figure S3.

In Figure 3b, the average saturation regime mobility is reported for the 0.05 and 5 mm/s coats, with current both parallel and perpendicular to the coating direction. By far the highest performing devices were those coated at 5 mm/s with parallel current, achieving a mobility of (2.3 ± 0.5) cm²/(V s) (\pm hereafter refers to the standard deviation among all measurements of a quantity). This value, as well as the observed $\approx 15\times$ charge transport anisotropy ($R_{0,90}$), is in good agreement with previous reports of devices fabricated with unidirectional coating techniques such as wire bar and brush coating, as highlighted in Table S1. Performance was unchanged after 6 months of storage in a nitrogen glovebox away from light, similar to previous reports.⁴⁴ Conversion of charge transport anisotropy to a value of S_{2D} can be performed through eq 2 in Figure 1, yielding $S_{2D,TFT}$ of 0.87 ± 0.04 . Thus, the sign of charge transport anisotropy for the 5 mm/s film agreed with the SE anisotropy, suggesting that charge transport was fastest along the direction of bulk backbone orientation. Surprisingly, the charge transport anisotropy of the 0.05 mm/s coating ($S_{2D,TFT} = 0.27 \pm 0.18$) did not match the bulk backbone orientation from SE (≈ -0.66). Although mobility in general was significantly lower for this low-speed coating, mobility was $\approx 2\times$ higher parallel to the coating direction versus perpendicular, even though SE indicated that backbones were preferentially oriented perpendicular to the coating direction. Since SE is a bulk measurement while TFTs are generally understood to be a surface measurement, this discrepancy can be sorted out through further structural characterization.

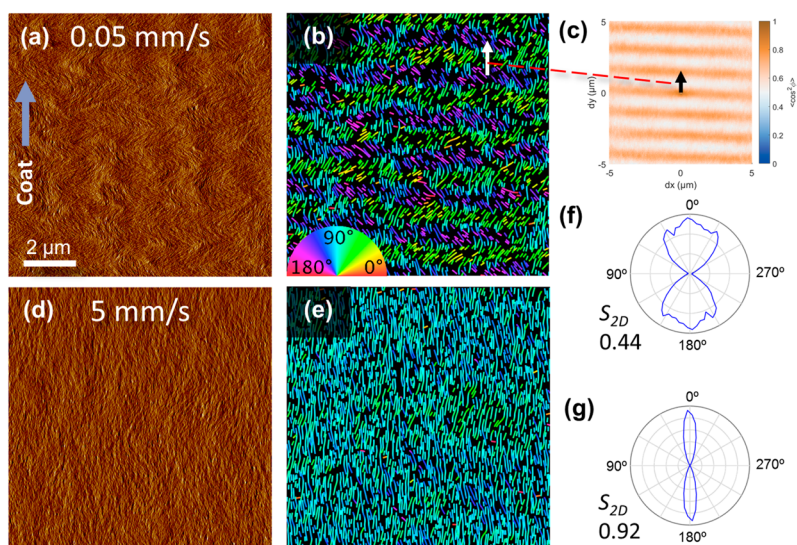


Figure 4. Tapping mode AFM phase channel micrographs and orientational analysis. (a) Phase image from 0.05 mm/s coat. (b) False-colored orientation map of the phase image in part a as extracted by GTFiber. In-plane orientation is colored according to the color wheel legend at the bottom left. (c) 2D orientation correlation function of the fibril segments (60 nm each) in part b. Color scale indicates the expected value of $\langle \cos^2 \varphi \rangle$ between any two fibril segments separated by a distance (dx, dy) . (d, e) Same images and analysis as in parts a and b but for the 5 mm/s coating. (f, g) Orientation distributions of fibril segments for the analyzed images from 0.05 and 5 mm/s coats, respectively. Each extracted fibril is broken into segments of equal length, each of which contribute a count to an angular bin. Varied orientations can be present along a single fibril backbone. The value of S_{2D} for each orientation distribution is reported at bottom left.

Surface Fibril Orientation. Charge transport in TFTs is a function of the active layer structure and energetic landscape within the first few nanometers of the dielectric interface.^{45,46} Top-gated TFTs thus represent one of the few cases where meaningful correlations can be drawn between surface imagery and mobility. N2200 has been shown previously to aggregate strongly in toluene, resulting in thin films with fibrillar domains observable via AFM imaging.¹³ We collected 10 μm AFM images from the surface of the blade-coated films and analyzed them using GTFiber orientational analysis software, as shown in Figure 4.²¹ Our AFM phase images reveal a fibrillar morphology at both high and low speeds; the height channel, available in the Supporting Information, Section S3, contains similar oriented features and indicates a relatively smooth surface with step sizes between ≈ 1 and 2 nm at fibril edges. The film coated at 5 mm/s contains fibrils whose long axes are strongly aligned with the coating direction (indicated in Figure 4a). This is quantified by the narrow fibril orientation distribution shown in Figure 4g and the accompanying high value of S_{2D} .

However, the morphological features of the 0.05 mm/s image (Figure 4a) (and many other images across the literature) are not necessarily obvious to the naked eye. A fast Fourier transform (FFT) can reveal whether periodicity exists in any preferential direction overall but lacks a length-scale-resolved quantification of feature/fibril orientation.⁴⁷ To quantify the observed orientation in images of fibrillar N2200, we have extended the functionality of GTFiber to calculate the 2D orientation correlation function (OCF) of the fibril backbones. Details of the calculation method can be found in Figure S7, but briefly, GTFiber is a MATLAB-based image analysis program, originally developed for AFM images of P3HT fibrils; it extracts and vectorizes fibril backbones, permitting the estimation of orientation distributions, fibril length and width distributions, and orientational order parameters.^{21,48} In Figure 4c, we have applied a standard algorithm for the calculation of the OCF to the extracted fibril backbone vectors shown in Figure 4b. This

yields a 2D map of $\langle \cos^2 \varphi \rangle$ versus dx and dy : the expected cosine of the in-plane angle between two fibril backbone vectors separated by a distance (dx, dy) . The results are spatially binned so that each bin represents the average correlation of every vector pair that is separated by (dx, dy) ; the counts for each bin are also duplicated and rotated 180° around the origin, ensuring rotational symmetry of the results. While the images are 10 μm across, the OCF only considers separations up to (5 μm , 5 μm), because noise due to undersampling occurs at separations greater than half the image size. There is no padding applied at the image boundaries such as reflection or periodicity; statistics are simply calculated across every pair of vectors contained within the image frame.

The film coated at 0.05 mm/s contains a periodic, almost sinusoidal fibril packing at the top surface—a morphological feature also observed in zone-cast PBTTT nanoribbons.⁴⁹ The associated orientation distribution in Figure 4f is broader, with peaks at $\approx 0^\circ$ (vertical, parallel to coating direction) and $\pm 30^\circ$. There are virtually no fibrils oriented horizontally. The OCF in Figure 4c has remarkable horizontal bands alternating between $\langle \cos^2 \varphi \rangle \approx 0.5$ and 1 at a wavelength of ≈ 1600 nm. As illustrated by the paired arrows between Figure 4b and Figure 4c, this means that fibrils separated vertically by 1600 nm should have similar orientation—but fibrils separated by 800 or 2400 nm should have $\langle \cos^2 \varphi \rangle \approx 0.5$. From the images, it is clear that the expectation value of 0.5 for $\cos^2 \varphi$ means that the average angle between fibril segments separated vertically by 800, 2400 nm, etc. is not random but has an orientation alternating by $\pm 45^\circ$. Since the horizontal correlation (along the dx direction) is strong, we can conclude that the surface fibrils for this sample are in horizontal bands with orientation alternating between $\approx \pm 22.5^\circ$ on average. This is strongly reminiscent of a smectic liquid crystalline phase, which colloidal rods are known to form.⁵⁰

Structural Model of N2200 Fibrils. Prior to discussing the relationship between the remarkably distinct surface fibril

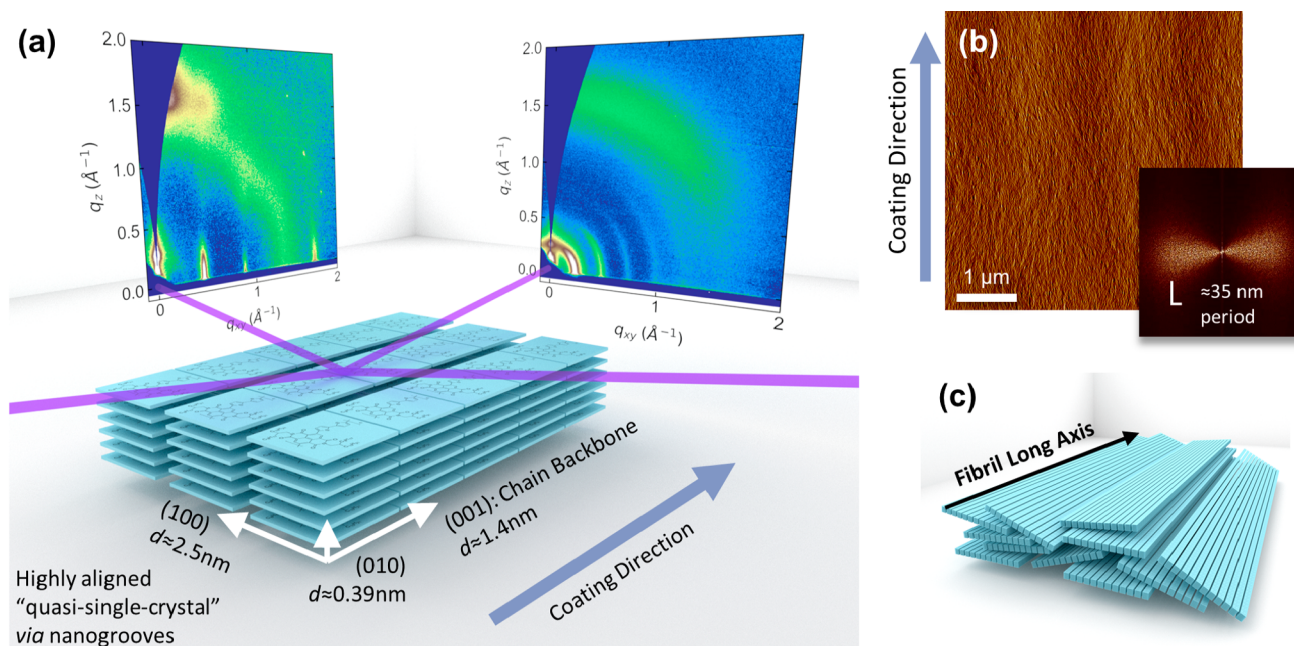


Figure 5. Crystal structure of N2200 fibrils. (a) GIWAXS patterns collected with the beam aligned parallel and perpendicular to the coating direction of a highly aligned thin film of N2200. (b) $5\ \mu\text{m}$ AFM phase image of N2200 thin film coated at 5 mm/s. Inset: Fourier transform of this image, revealing horizontal periodicity with a predominant pitch of 35 nm. (c) Schematic of “disordered logs” bulk crystal packing.

orientation distributions and charge transport, we must determine the structure (shish versus kebab) of the fibrils themselves. Trefz et al. recently provided strong evidence that fibrils of N2200 aggregate in the shish motif, i.e., polymer backbone parallel to the fibril long axis.²⁴ This was determined through a combination of TEM, AFM, and NEXAFS of anisotropic blade-coated films. We present here a combination of GIWAXS, AFM, and NEXAFS, which together enable the characterization of both in- and out-of-plane crystal orientation, in-plane surface fibril orientation, and in- and out-of-plane backbone orientation at the top and bottom surfaces. This is intended as both a confirmation and extension of Trefz’s results and as a backdrop for analysis of the *in situ* data in a later section.

It is clear from the different correlations between fibril anisotropy and bulk (SE) anisotropy that we must allow for vertical gradients in the film order, complicating correlations between the most detailed structural tool, GIWAXS, and the surface fibrils. To minimize the influence of vertical gradients in the in-plane order, we fabricated a highly aligned quasi-single-crystal thin film by blade coating N2200 from toluene at 5 mm/s on SiO_2 substrates patterned with nanogrooves parallel to the coating direction, as described in previous publications.^{17,51} We note that the nanogrooved substrate was used only for the development of this structural model and not for measuring the development of N2200 orientation in other sections of this Article. High-accuracy total electron yield (TEY) NEXAFS and GIWAXS were performed on this sample.

The details of the NEXAFS measurements are given in the Supporting Information, Section S5. TEY NEXAFS is surface sensitive, probing the top $\approx 3\ \text{nm}$ of the film. Measurements were made at both the air interface and the buried interface, exposed by floating films off of their original substrate in deionized water and picking them up on a small piece of bare silicon (native oxide). The air interface of spin-coated and zone-coated N2200 has recently been detailed by Schuettfort et al. revealing a distinct shift in the alignment of the carbon-edge, $\pi-\pi^*$

transition dipole moment (TDM) from face-on in the bulk (transmission NEXAFS) to edge-on at the surface (TEY NEXAFS).⁵² We find similar trends for the air versus buried interfaces of films cast on untreated and nanogrooved substrates. The in-plane order (S_{2D}) for the $\pi-\pi^*$ at the air interface is found to be independent of substrate, comparable (≈ -0.8) to that of the AFM fibrils in magnitude and of opposite sign, consistent with the $\pi-\pi^*$ TDM being perpendicular to the backbone. The S_{2D} of the buried interface on the untreated substrate was ≈ 0.0 , while that of the nanogrooved substrate was intermediate between the two limits. The NEXAFS unambiguously confirms that the surface fibrils are shish, with backbone along the long fibril axis. NEXAFS also encodes the orientation of the TDM with respect to the surface normal (the tilt of the conjugated plane). At the air interface, $\langle \cos^2 \theta \rangle$ is ≈ 0.24 independent of substrate, corresponding to a tilt (for a narrow ODF) of 61° . Vertical gradients are not completely eliminated in the quasi-single-crystal film, as $\langle \cos^2 \theta \rangle \approx 0.20$ (idealized tilt of 47°) at the film bottom. The 14° difference in tilt between top and bottom is the same as that reported for the top versus bulk of spun films.

GIWAXS patterns collected from the quasi-single-crystal sample are presented in Figure 5a alongside a $5\ \mu\text{m}$ AFM phase image in Figure 5b. The Fourier transform of the AFM image reveals strong periodicity perpendicular to the coating direction at a $\approx 35\ \text{nm}$ pitch, providing confirmation (beyond that of the GTFiber analysis) that fibril backbones align parallel to the coating direction at high speed.

GIWAXS patterns were collected with the incident beam parallel and perpendicular to the coating direction, as illustrated in Figure 5a. These measurements were part of a full in-plane rotation scan available in Figure S8. With the incident beam parallel to the fibril long axis, the scattering vector q probes diffraction perpendicular to the fibril long axis, in both the in-plane and out-of-plane directions. Along the in-plane q_{xy} -axis, one observes the ($h00$) progression, characteristic of the

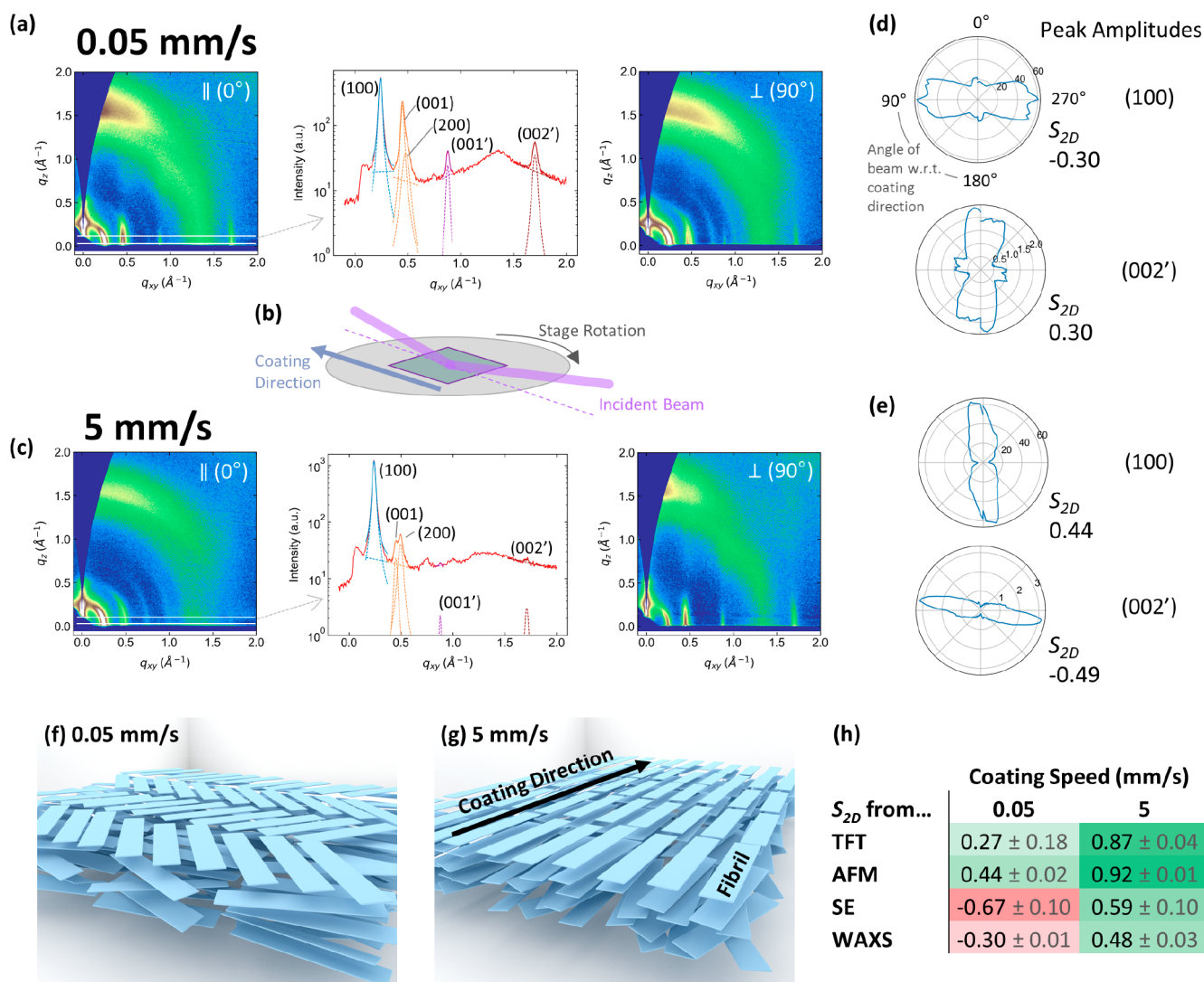


Figure 6. In-plane pole figures for blade-coated thin films of N2200 fibrils. (a) Results for 0.05 mm/s coating speed: GIWAXS patterns with incident beam parallel and perpendicular to the coating direction as well as in-plane line profile with fitted diffraction peaks. (b) Schematic illustration of X-ray scattering experiment: when the incident beam is parallel to the coating direction, this corresponds to an angle of 0° . (c) Results for 5 mm/s coat, same as part a. (d, e) Distribution of (100) and (002') peak amplitudes (fitted to in-plane line cuts) with respect to the angle between the incident beam and coating direction. 0° indicates parallel orientation and 90° perpendicular; in other words, the coating direction is vertical for these two plots. (f, g) Schematic illustrations of the fibril packing for both the 0.05 and 5 mm/s samples. (h) Table of S_{2D} values from each characterization source in this study, for both samples (\pm values indicate standard deviation among at least three independent measurements).

lamellar stacking of N2200 at a d -spacing of $\approx 25 \text{ \AA}$. A broad π - π stacking peak is visible along the out-of-plane q_z -axis at $\approx 1.6 \text{ \AA}^{-1}$. The out-of-plane angular distribution of these peaks indicates a predominantly face-on orientation but with a moderate amount of “roll”: $\langle \cos^2 \psi \rangle$, where ψ is the angle between the (100) director and the surface normal at this in-plane rotation, which was calculated as ≈ 0.2 ⁵³ with the beam parallel to the coating direction. We note that this does not necessarily imply a perfectly “face-on” orientation of the conjugated rings in the unit cell: backbones could have a tilted orientation, similar to that observed for PBTTT, but still pack with the (100) lattice vector in the q_{xy} plane.⁵⁴

With the incident beam perpendicular to the fibril long axis, the peaks arising from polymer backbone scattering are dominant (the (00 l) series) and strongly confined to an in-plane orientation, indicating that the crystals lie flat along this axis with little out-of-plane tilt, consistent with the SE. This is confirmed by the narrower out-of-plane distribution of the π - π

stacking peak about the surface normal. The in-plane confinement of the polymer backbone lattice vector could be due to it being the long axis of the crystal habit, thereby limiting its rotational freedom in comparison with the lamellar stacking vector. This suggests that the bulk crystals are fibrillar in nature, although we emphasize that fibrils are only directly observed by AFM at the surface. Operating under the assumption that the bulk crystals are in fact fibrillar, a schematic illustration of the bulk N2200 crystals reflecting these scattering features is provided in Figure 3c. Taken together, these data paint the picture of “shish-style” bulk fibrils (backbone parallel to the fibril long axis) lying face-on with moderate roll about the (001) axis but very little tilt about the (100) axis. This structural model is consistent with the alignment we observe in the bulk backbones via SE and the fibril alignment observed via AFM. We note that the NEXAFS requires the orientation about the backbone axis to be different for the bulk and surface fibrils. The difference in $\langle \cos^2 \theta \rangle$ is small compared to the $\langle \cos^2 \psi \rangle$ observed in GIWAXS.

Thus, the surface fibrils may simply be slightly less disordered than the bulk. This, however, would require the counterintuitive conclusion that the conjugated plane is tilted $\sim 28^\circ$ from the $\langle 010 \rangle$! The N2200 backbone is torsionally structured due to steric hindrance about the carbonyls; a unique reconciliation of the NEXAFS and GIWAXS giving the molecular tilt in the unit cell has not been made.⁵² In the structurally similar polymer P(NDI-SVS), diffractive X-ray waveguiding has demonstrated that crystalline material at the surface exists in a ≈ 5 nm thick skin with orthogonal [(100) along the surface normal] orientation to the face-on [(010) along the surface normal] bulk. Previous measurements on spun N2200⁵² (Schuettfort) and our measurements on blade-coated N2200 were unable to resolve a distinct crystalline surface layer. The combined NEXAFS and GIWAXS results are most consistent with fibrillar texture for both the surface (total material) and bulk crystals with both fibrils shish. Bulk material exhibits a face-on (both $\langle 100 \rangle$ and $\langle 001 \rangle$ in the surface plane) texture with mild disorder about the backbone director, while surface material exhibits a distinct, more edge-on texture with unquantified crystal content.

Crystalline Texture and in-Plane Crystal Orientation. A fortunate side-effect of the bulk face-on texture of N2200 is that both its lamellar stacking and chain backbone peaks lie in the plane of the substrate and are thus prominent in line cuts along the q_{xy} -axis of GIWAXS patterns. Most semiconducting polymers pack with an edge-on orientation, so the π - π stacking peak has the strongest in-plane presence—however, this high- q peak is typically broad and strongly affected by background scattering sources. The multitude of strong low- q peaks generated by N2200 presents an opportunity to create high-resolution in-plane pole figures for many of the lattice vectors, which we have done by collecting GIWAXS patterns at 3° intervals from blade-coated films of N2200 mounted on a rotary stage, illustrated in Figure 6b. Figure 6 shows the results of these in-plane pole figures for films coated at 0.05 and 5 mm/s, for which we earlier presented backbone orientation, charge transport anisotropy, and surface fibril orientation distributions. These films have a vertical gradient in in-plane orientation, as revealed in NEXAFS. This is manifested through the simultaneous presence of lamellar and backbone peaks in the parallel (0°) and perpendicular (90°) patterns, as shown in the line profiles in Figure 6a,c. Through peak fitting on these line profiles, we obtained the amplitudes of the (100), (001), (200), (001'), and (002') peaks as a function of in-plane sample rotation. The (001') peaks were originally assigned by Rivnay et al., which he described as originating from a different backbone polymorph than that of the (001), despite their positions agreeing with a hypothetical series of higher-order peaks.⁵³ Indeed, the peak intensities of the (001) progression do not appear to decrease monotonically as would be expected for a conventional series of higher-order peaks. We thus adopt Rivnay's nomenclature here. Trefz assigns (001), (002), and (004) to the peaks we label (001), (001'), and (002') yet similarly does not observe what would be the (003) peak in any of their samples.²⁴ The raw pole figure data for all samples are available in the Supporting Information, Section S4.

In Figure 6d,e, we present the orientation distributions of the (100) and (002') peak amplitudes for the 0.05 and 5 mm/s samples, respectively. The (002') peak was chosen instead of the (001) because the (001) and (200) overlap strongly at the intermediate rotations. The stage was rotated through 180° of in-plane orientation, so data are duplicated and rotated by 180° to form a continuous plot; note that 0° is at the north pole of the

polar plots for consistency with the AFM figures. For both coating conditions, the maxima in the (100) and (002') do not occur at 90° , implying that the in-plane crystallographic angle, β , is not 90° , and the crystal structure is, at most, monoclinic. Nevertheless, the shape of these distributions agrees with the structural knowledge gained from the previously presented data. For the 5 mm/s sample, given that both SE and AFM indicated a strong alignment parallel to the coating direction for backbones and fibrils, respectively, one would expect a strong (100) peak with the incident beam parallel to the coating direction (0°) and a strong (002') peak with the incident beam perpendicular to the coating direction (90°), which is what we observe.

For the 0.05 mm/s sample, SE indicated that bulk backbones were aligned perpendicular to the coating direction, but AFM indicated that surface fibrils were aligned mostly parallel. The WAXS pole figures reconcile both of these data sources: the majority population of crystalline material is oriented with backbones perpendicular to the coating direction (strong peaks in (100) and (002') at 90° and 0° , respectively), but a minority mode of crystals have backbones parallel to the coating direction (small peaks in (100) and (002') at 0° and 90° , respectively). This suggests that the wavelike fibrils observed via AFM for the 0.05 mm/s sample are part of a very thin layer (perhaps monolayer) at the surface, while the bulk of the material in the film (crystalline and amorphous) is oriented perpendicular to the coating direction. Taking all of this structural data into account, illustrations of the fibril packing for these two samples are presented in Figure 6f,g. We again adopt the assumption that the crystal and fibril populations are mostly overlapping and that fibrils are distributed uniformly through the depth of the films.

Structure–Property Correlations. In Figure 6h, we compute and compare in-plane anisotropy in terms of S_{2D} for all the measurements performed in this study. The values for the OFET measurements were derived using eq 2 in Figure 1, assuming the mobility is a simple linear response tensor, using the ratio of the parallel versus perpendicular mobilities as $R_{0,90}$. The values for AFM were calculated via GTFiber and averaged across three images from each sample. The values for GIWAXS were calculated using eq 1 in Figure 1 on the amplitudes of the (100), (001'), and (002') peaks; these three values of S_{2D} were then averaged. Three key features of this data set emerge: The first feature is that the TFT mobility anisotropy measurements agree with AFM anisotropy for both samples. The second feature is that the NEXAFS (surface sensitive, total average) and SE (bulk, total average) anisotropy are less than the AFM. The SE versus NEXAFS difference is consistent with a decrease in anisotropy moving away from the air interface. The NEXAFS versus AFM difference suggests the presence of less ordered material, either between the fibrils or within the fibrils. The third key feature is that the GIWAXS anisotropy is significantly weaker in magnitude than the SE anisotropy for both samples. This suggests that the crystalline material is less aligned than the bulk material. Since the crystalline material is a subset of the bulk, the difference must be due to noncrystalline material: either a highly aligned amorphous phase or highly aligned noncrystalline aggregates. In either case, it indicates that the overall degree of crystallinity may be low. This result is somewhat counterintuitive but can be further elucidated by examining the alignment mechanism for this system through *in situ* measurements, presented below.

The quantitative agreement between the TFT S_{2D} and the AFM S_{2D} for the 5 mm/s film is quite striking. This is qualitatively consistent with the demonstrated shish structure of

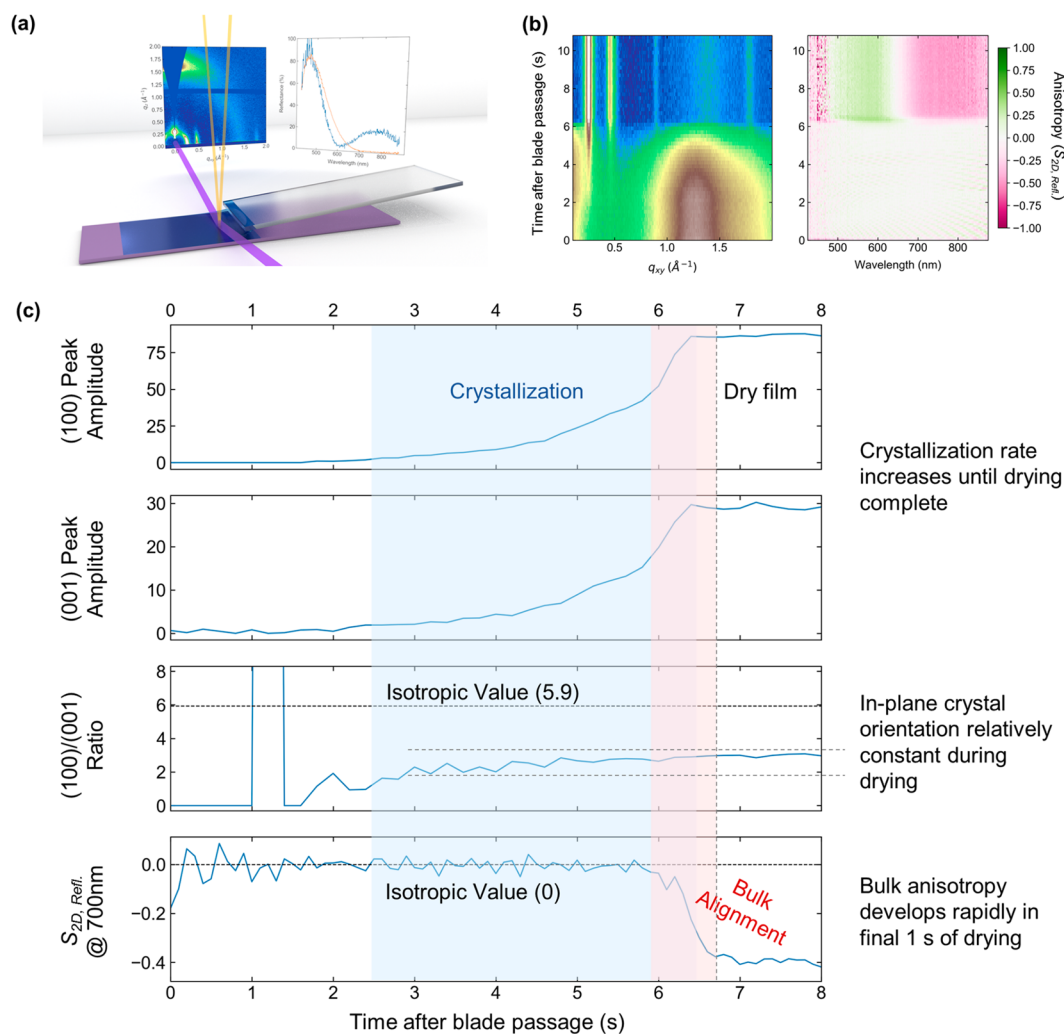


Figure 7. *In situ* characterization of a blade-coated N2200 thin film (5 mm/s). (a) Schematic of experimental setup and raw data collection. (b) Raw line cut data from WAXS patterns and calculated S_{2D} for all wavelengths of raw UV-vis reflectance data versus time after blade passage (vertical axis). (c) Amplitude of the (100) peak and (001) peak from peak fitting of each collected pattern, the ratio of the (100)/(001) peak amplitudes, and S_{2D} from UV-vis reflectance at 700 nm versus time after blade passage in seconds.

the fibrils and the assumption that the fast transport direction is along the conjugated backbone and is quantitatively consistent with the simple, diffusive transport model proposed by Sirringhaus.⁵⁵ This simple, 1:1 relationship between μ and backbone orientation is rarely observed (and is not found in the 0.05 mm/s film).

It is interesting to reflect upon the significant reduction of the absolute mobility values for the low-speed case (and lower anisotropy). The mobility perpendicular to the coating direction at 0.05 mm/s was $(0.22 \pm 0.06) \text{ cm}^2/(\text{V s})$, similar to the value for 5 mm/s: $(0.16 \pm 0.03) \text{ cm}^2/(\text{V s})$. Oddly, however, the mobility parallel to the coating direction for the low-speed film was only $(0.38 \pm 0.10) \text{ cm}^2/(\text{V s})$, even though the surface fibrils were relatively aligned in that direction ($S_{2D,AFM} = 0.44 \pm 0.02$). This is in stark contrast to the observed anisotropy for the high-speed case ($S_{2D,AFM} = 0.92 \pm 0.01$). It is possible that the periodic, high-angle ($\approx 45^\circ$) fiber-fiber grain boundaries that charges would encounter due to the wavelike structure in the low-speed sample act as an extra impediment to charge transport, beyond the hindrance due simply to weaker alignment.¹² The simple diffusion model of Sirringhaus treats grain boundaries solely as material with a different orientation

and does not allow for different local mobilities. While the adjacent fibril-fibril structure of the 5 mm/s surface can support facile charge transport, likely due to linear-extended tie chains terminating in both fibrils, the 45° bend in the 0.05 mm/s films implies significant local backbone disorder/torsion.

***In Situ* Characterization of Orientation.** Having presented an understanding of N2200 fibril structure and tools to quantify its orientation, we address the kinetics of formation of these structural features with *in situ* measurements. In this experiment, we blade-coated a thin film of N2200 from a 20 mg/mL toluene solution at 5 mm/s on an 8 mm wide SiO_2 substrate at a synchrotron beamline. We also attempted this experiment with the 0.05 mm/s film, but it was evident that the majority of drying and structural organization occurred while the blade was still obstructing the path of the incident X-ray beam. Given that 5 mm/s was the higher-performance case and that previous authors have also had success coating in the LLD regime, we found this to be the most relevant experiment to run and analyze. The GIWAXS pattern was collected at 200 ms intervals with the incident beam perpendicular to the coating direction—i.e., the same configuration as the 90° pattern from Figure 6c. At the same time and position on the substrate, split-polarized UV-vis

reflectance measurements were collected at 100 ms intervals, giving an indication of wet film thickness and bulk backbone orientation. The results from these multimodal measurements are presented in Figure 7: Figure 7a illustrates the experimental configuration and raw data collected. Figure 7b shows the intensity of the in-plane line cut from GIWAXS (the same in-plane cut presented in Figure 6) plotted over time (the vertical axis), with $t = 0$ being the time immediately after the blade had fully passed through the beam. This event was very clear in both the X-ray and UV-vis data and provided a simple way to synchronize the multiple channels. A real-time video of the raw data can be found as a file in the Supporting Information.

Alongside the WAXS line cuts is the UV-vis anisotropy parameter calculated at each wavelength over time, defined as

$$S_{2D,refl.} = \frac{R_{0:90} - 1}{R_{0:90} + 1} \quad (1)$$

as in eq 2 in Figure 1, but where

$$R_{0:90} = \frac{-\log(\text{refl}_{\parallel})}{-\log(\text{refl}_{\perp})} \quad (2)$$

using $-\log(\text{reflectance})$ as a stand-in for absorbance. The reflectance convolves both information on the dielectric function (real and imaginary parts) of the film with interference effects due to the film thickness. It is thus not directly interpreted as dichroism as is evident in Figure 7b where the magnitude of reflectance anisotropy changes sign from low to high wavelengths. However, the presence of anisotropy (any value other than 0) is unambiguous. In this analysis, we use the reflectance anisotropy only to determine the presence and timing of bulk backbone orientation—we do not attempt to use this quantitatively, already having this information from the static film SE.

As seen in Figure 7b, the WAXS line cuts are dominated at an early time by a strong solvent halo between ≈ 1.0 and 1.5 \AA^{-1} . However, streaks from the emergence of the (100) and (001) peaks are apparent as early as ≈ 2 s after blade passage at ≈ 0.25 and $\approx 0.45 \text{ \AA}^{-1}$, respectively. These early peaks could be a result of crystallization of aggregates already formed in solution or nucleation of new crystals (or both). Fitted peak amplitudes were obtained as described in Figure 6. Since we can only obtain data with the incident beam perpendicular to the coating direction (again, the equivalent of the 90° pattern in Figure 6c), we cannot measure full orientation distributions. However, we can use the ratio of the (100)/(001) peaks to estimate in-plane crystal orientation from a single pattern. This is a unique feature of N2200 due to its face-on texture, which is maintained throughout the drying process: $\langle \cos^2 \psi \rangle$ for the (100) peak remains below ≈ 0.25 after 2 s (see Figure S11). For a perfectly aligned sample such as that in Figure 5, the (100)/(001) ratio should approach infinity at 0° and zero at 90° . To calibrate this metric, we need to know the ratio for an isotropic sample. We simulated powder diffraction patterns for N2200 by summing the WAXS patterns for available rotation scans: in addition to those from Figure 6, there were data available from the highly aligned sample in Figure 5 and a near-isotropic sample coated at 0.1 mm/s. The fitted (100)/(001) peak ratio averaged across these four simulated powder patterns was 5.9 ± 0.2 , shown in Figure S9. Thus, with the incident beam perpendicular to the coating direction, values of the (100)/(001) ratio below 5.9 suggest crystals oriented with backbones parallel to the coating

direction, and values above 5.9 suggest perpendicular orientation.

All of these structural metrics are plotted in Figure 7c on a common time axis, including the (100) and (001) amplitudes, the (100)/(001) ratio, and $S_{2D,refl.}$ at 700 nm. The growth of both the (100) and (001) peaks is slow at first but rises more quickly in the final ≈ 2 s of film drying, which appears to conclude at ≈ 6.5 s. This indicates an increasing rate of crystallization up until drying is complete, which could be attributed to Johnson–Mehl–Avrami isothermal crystallization kinetics; in this case the typical sigmoidal growth curve is cut short by arrested molecular transport due to the rapid solidification of the wet film.⁵⁶ The (100)/(001) ratio, which should only be considered valid after ≈ 2 s due to the low signal-to-noise ratio prior to that point, increases from an initial value of ≈ 2 to a final value of ≈ 3 . These values are both well below the isotropic value of 5.9, suggesting that the crystalline population is oriented with chain backbones parallel to the coating direction throughout the entire drying process. There is very little fluctuation in this ratio in the final two seconds of drying (≈ 4.5 – 6.5 s), indicating that the final *in-plane* crystal orientation is locked in well before drying is complete. It should be noted, however, that this value of the (100)/(001) ratio is slightly higher (slightly more isotropic) than that observed in films coated at the same conditions in our lab, rather than at the beamline. This may be due to a combination of substrate edge effects (narrower substrates were used for the *in situ* runs) and differences in the convective air flows affecting film drying rates.

The drop in $S_{2D,refl.}$ from ≈ 0 (isotropic) to ≈ -0.4 is noteworthy because it occurs so late in the drying process; indeed, it is the last structural change to occur before all activity ceases at ≈ 6.5 s. This was so unexpected that we reran more coating experiments at 5 mm/s on a glass slide in transmission mode (although not at a beamline and thus without simultaneous GIWAXS) to track the true absorbance dichroic ratio as a function of drying time. Even in these experiments, the UV-vis anisotropy did not develop until within the final second of drying (see Figure S10). This is remarkable for two reasons: it indicates that (1) the majority of the N2200 does not align until the final second of drying but also that (2) the majority of N2200 is not crystalline. It is important to note here that while GIWAXS is sensitive only to crystalline material, the UV-vis anisotropy is sensitive to all N2200 chains, regardless of their crystallinity. This indicates that the early aligned crystalline population is so small that it does not register in the UV-vis measurement; the bulk backbone population remains isotropic for almost the entire crystallization process. Furthermore, given that (1) the early crystal population is small, and (2) the diffraction peak amplitudes increase no more than $2\times$ during the late time bulk alignment phase, it appears that the majority of material aligning in the bulk alignment phase is not participating in crystallization. One possible explanation for this is that the amorphous N2200 chains pass through a lyotropic liquid crystal phase transition once a critical amount of solvent has evaporated, and the orientation of this liquid crystal phase templates off of the small population of aligned crystals, or, alternatively, that both the crystals and free polymer backbones template off of a small population of aligned noncrystalline aggregates (fibrils). If such a transition were taking place, we estimate that it occurs at a volume fraction of $55\% \pm 15\%$ N2200, based on an analysis of film thickness from the reflectivity data, presented in Figure S12. A liquid crystal phase transition would be in agreement with the mechanism proposed by Trefz et al.²⁴ Considering the fact that

the material at the air interface is the most highly aligned material in the film (highest S_{2D} evident in AFM and NEXAFS), these results suggest that fibrils at the air interface template the alignment of crystalline and noncrystalline material in the bulk.

It is difficult to draw entirely generalizable conclusions about such a complex system, but the following seem to be supported by the nascent research on blade-coating-aligned semiconducting polymers.

- (1) Noncrystalline polymers (amorphous material) may contribute more to observed bulk alignment than crystalline material. This is borne out in the current study by the higher magnitude of S_{2D} for measurements of all backbones versus measurements of crystals. Shaw et al. performed a study of blade-coated P(DPP3T) in which bulk polymers showed strong anisotropy (UV–vis dichroic ratio of ≈ 7), but crystals showed weaker or even contradictory π – π stacking anisotropy in GIWAXS.¹⁸ A follow-up study confirmed that films displaying the highest in-plane bulk alignment had comparatively low relative degrees of crystallinity versus other coating speeds.²³
- (2) Bulk polymer alignment tends to template off of other oriented objects. While crystals seem to be a minority population of aligned material, their presence is still important to alignment in many cases. The data presented here offers unambiguous evidence that crystals developed preferential orientation prior to bulk polymer alignment. Shaw attributed the varying degree of bulk alignment of P(DPP3T) to competition between ordered crystal nuclei at the substrate and disordered nuclei at the air interface. Wu et al. observed depth-dependent gradients in polymer backbone orientation in blade-coated films of PCDTPT and CDTBTZ, with bottom-up templating provided by nanogrooved substrates and top-down templating apparently provided by oriented fibrils at the air interface.¹⁷ In many cases, the degree of anisotropy seems to decrease with increasing separation from the templating material. Without nanogrooves, Wu observed nearly isotropic polymer backbones at the buried interface, mirroring the behavior of our 5 mm/s film. Persson et al. found that blade-coated films from aggregated P3HT solutions contained nanofibers with higher anisotropy at the air interface than at the substrate.²¹
- (3) Predicting the direction of polymer and fibril orientation (parallel or perpendicular) remains complex. Shaw's studies saw P(DPP3T) backbones align parallel to the coating direction only at intermediate blade speeds. In a study of blade-coated P(DPP2T-TT) in the evaporative regime, Qu et al. found that shish-style fibrils oriented parallel to the coating direction at the surface but moderately perpendicular in the bulk, similar to the 0.05 mm/s film presented here.²² The conflicting orientations were attributed to extensional flow at the air interface versus shear flow in the bulk. In Wu's study, backbones aligned perpendicular to the coating direction in the evaporative regime; as coating transitioned to the LLD regime, backbones aligned parallel, and at speeds above 10 mm/s, a return to an in-plane isotropic film was observed. This behavior is similar to that of N2200 in terms of the progression of orientation with increasing blade speed (Figure 2a). One possible explanation for the return to

isotropic films at high speeds is that the increased solvent evaporation time due to the thicker wet film allows for randomization of seed crystal orientation—i.e., a loss of memory of blade passage, resulting in a liquid crystal phase transition with a less-oriented template. The complex interplay of flow, transport, and confinement effects that gives rise to these varied orientations will certainly be the subject of further study, along with a more detailed characterization of the kinetics of crystallization and alignment during film drying.

CONCLUSIONS

We have presented a comprehensive characterization of blade-coated N2200 for TFT applications, including significant detail in the measurement of in-plane orientation and alignment from multiple structural data sources. N2200 displays the expected power-law dependence of film thickness on blade speed in both the evaporative and LLD regimes. However, bulk polymer alignment flips from perpendicular to the coating direction to parallel as blade speed increases. The anisotropy of top-gate TFT mobility did not agree with the bulk backbone orientation; rather, mobility anisotropy was strongly correlated with the in-plane alignment of the fibrillar morphology at the surface, quantified through AFM image analysis. We also observed a striking periodic, wavelike packing of N2200 fibrils at the air interface for low blade speeds and quantified this morphology with a custom orientation correlation algorithm that extends the functionality of GTFiber image analysis software. The high-angle grain boundaries present in this structure appeared to impede charge transport despite an overall high degree of fibril alignment.

Through the analysis of a nanogroove-aligned thin film in conjunction with high-resolution in-plane GIWAXS pole figures, we developed a model of crystal orientation for N2200 thin films. While the bulk crystal population for high-speed-coated films was aligned in agreement with optical and AFM results, the crystal population in low-speed films was aligned perpendicular to the coating direction but with a bimodal character suggesting conflicting surface and bulk populations. We used the model of crystal anisotropy to analyze simultaneous *in situ* GIWAXS and UV–vis reflectance data from N2200 thin films coated at 5 mm/s. The data suggest that a small population of crystals that orient early in the drying process template bulk alignment that occurs very late in the drying process and, furthermore, that the majority of aligned material in N2200 thin films is not crystalline at these conditions. Bulk alignment was likely established through a lyotropic liquid crystalline phase.

Importantly, we have demonstrated the utility of S_{2D} as a general and quantitative metric to describe and compare in-plane orientation distributions of structural features and electrical properties for oriented thin films of conjugated polymers. This metric can be easily approximated from ratio-based representations of anisotropy, while mitigating the inherent sensitivity and nonlinearity of such ratio-based approaches. These results should further the rational design of aligned semiconducting polymer thin films for high-performance TFT applications.

METHODS

Materials. P(NDI2OD-T2) (N2200) was obtained from Polyera and used as received without further purification. Toluene was obtained from Sigma-Aldrich. CYTOP CTL-809 M was obtained from Bellel and used as received without further purification.

Solution Preparation. Solutions were prepared in a nitrogen glovebox at 20 mg/mL by dissolving 10 mg of polymer in 2 mL of toluene (Sigma) in 5 mL borosilicate amber glass vials, tightly capped, and heated to 60 °C for 1 h to ensure complete dissolution. No stir bar was used; solutions were gently swirled to remove solid particles from the vial walls. After cooling to ambient conditions, the solutions were allowed to age inside the glovebox for at least 24 h before films were coated.

Thin Film Preparation. Films of N2200 were coated from room temperature solutions on clean Si substrates with a native oxide layer in a nitrogen glovebox. For structural measurements, Si substrates were used as received from the manufacturer without further cleaning. Blade coating was performed with a custom apparatus described previously.⁵⁷ Pre-cleaned glass microscope slides were blown dry with nitrogen and used as blades. The blades were held at an angle of $\approx 10^\circ$ off the horizontal and a gap height of 200 μm and were wetted with 25 μL of solution using a 50 μL glass syringe (Hamilton). The substrate was held at 30 °C. For spectroscopic ellipsometry samples, a coating program was initiated to generate strips of film at five different velocities per Si substrate. Coating velocities were staggered between slides such that the first slide had films coated at 0.05, 0.15, 0.42, 1.2, and 3.5 mm/s, while the second slide had films coated at 0.085, 0.25, 0.71, 2.1, and 5.9 mm/s, so that, when merged, the coating velocities spanned a wide range with logarithmic spacing. Additional points were collected at 10 and 20 mm/s, which required significantly more “runway” to obtain a fully developed film. For GIWD samples, including in-plane pole figures, only one coating speed was used per substrate.

Spectroscopic Ellipsometry. Film thickness and anisotropy were extracted from spectroscopic ellipsometry using a J.A. Woollam Co., Inc., M2000 instrument, performed on thin films on Si substrates. Incident angles of 50°, 60°, and 70° were used with 2 s exposure times. Full Mueller Matrix data were collected with the coating director at 0°, 45°, and 90° relative to the incident beam. A biaxial optical model with parametrized absorption spectra was fitted to the rotation scan data, yielding both film thickness and a dichroic ratio at 700 nm. Full model parameters and fitting results can be found in the Supporting Information, Section S1.

TFT Device Fabrication. TFT devices with top-gate, bottom-contact architecture were fabricated for the electrical characterization of thin films blade-coated from the as-prepared solutions. Glass microscope slides diced into 25 mm \times 25 mm squares were used as substrates and were sonicated for 10 min each in CHCl_3 and isopropanol, followed by a 10 min UV–ozone treatment before use. Cr/Au contacts were evaporated onto the glass slides by thermal evaporation through a shadow mask at a rate of 0.1 nm/s, resulting in a ≈ 5 nm Cr adhesion layer and ≈ 50 nm Au. Thin films of N2200 were deposited via blade coating at 0.05 and 5 mm/s, as described above. The devices were then heated to 110 °C for 5 h; we refrain from calling this an “annealing” step because no significant structural changes occurred; rather this step was necessary to drive off excess solvent trapped at the buried interface. CYTOP (CTL-809M, Bellex) was used as the gate dielectric; it was deposited via spin coating as a pure material (no diluting solvent) at ≈ 942.5 rad/s (9000 rpm) with a 15 s ramp, affording films of ≈ 650 nm thickness as measured by SE. Another 5 h, 110 °C heat treatment was applied after this step to cure the CYTOP. Finally, a top-gate shadow mask was aligned with the bottom contact electrodes and clamped onto the substrate, and ≈ 100 nm Al electrodes were deposited at 1.0 nm/s to avoid overheating the prepared devices.

Electrical Characterization. Individual OFET channels were tested with a custom automated probe station with nitrogen purge (Cascade Microtech). Transfer and output curves were measured by source measure units (Keithley 6430) controlled by LabVIEW software. The field-effect electron mobility (μ) was calculated in the saturation regime of transistor operation ($V_{\text{DS}} = +60$ V) by fitting the following equation to a plot of drain current (I_{DS}) versus gate voltage (V_{G}):

$$I_{\text{DS}} = \frac{WC_{\text{OX}}}{2L} \mu (V_{\text{G}} - V_{\text{th}})^2$$

where W (1000 μm) and L (50 or 100 μm) are the transistor channel width and length, respectively, V_{th} is the threshold voltage, and C_{OX} is the capacitance per unit area of the CYTOP dielectric ($K = 2.1$). The saturation regime equation was fitted between 40 and 60 V on the forward sweep. At least seven devices were used to compute the average mobility for each coating condition and electrode orientation. Additional information and raw data can be found in the Supporting Information, Section S2.

Atomic Force Microscopy. Thin film surface morphology was characterized with a Bruker Dimension Icon atomic force microscope operating in tapping mode with silicon probes (NanoSensors PPP-NCL-50, 21–98 N/m, 146–236 kHz). Images were collected at a 10 μm scan size with 512 samples per line at 1 line/s and the coating direction vertical in the image frame. Preprocessing was performed with the nanoscope Python library and included a third-order flattening operation before exporting the image as a PNG with no additional labels or overlays. These image files were analyzed using GTFiber, described in a previous publication, with a custom MATLAB function for orientation correlation function analysis, described in the Supporting Information, Section S3.²¹ Filter parameters included a 10 nm Gaussian smoothing, 60 nm orientation smoothing, 5 s diffusion time, 80 nm top hat filter, adaptive thresholding, 3000 nm² noise removal, 80 nm fringe removal, 60 nm fiber step length, 80 nm gap stitching, 5 μm^{-1} max curvature, and no minimum fiber length.

GIWAXS Characterization. X-ray scattering patterns for Figures 5 and 6 (in-plane pole figures) were collected at the National Synchrotron Light Source II (NSLS-II) beamline 11BM-CMS with a custom rotational stage. To ensure minimal wobble of the sample normal with respect to the scattering plane, the stage had a two cradle goniometer on top of the main rotation stage. To ensure the sample stayed centered during rotation, an x – y positioner was under the two cradle goniometer. The addition 4 degrees of freedom (beyond conventional GIWAXS) were remote controlled, allowing alignment via the specular X-ray beam to better than 0.005°. To ensure equal scattering volumes at all sample rotations, the films were formed into circles by placing them on a spin coater and wiping the edges with a CHCl_3 -soaked TexWipe folded into a sturdy corner. No differences in the scattering patterns were observed before and after this wiping process to suggest that solvent vapor annealing had occurred. Patterns were collected by a Photon Science CCD (1042 \times 1042 pixels, 101.7 μm \times 101.7 μm pixel size) area detector at a beam energy of 11 keV in a vacuum environment with 15 s exposure time and an angle of incidence of 0.14°. Sample–detector distance was approximately 227 mm from the sample center, and calibration was performed with a silver behenate standard. Calibration, data reduction, and analysis were performed in Jupyter Notebooks with a Python 3.6 Anaconda environment including the Numpy, Pandas, Matplotlib, pyFAI, and pygix libraries.⁵⁸

In Situ Characterization. Data for Figure 7 were collected at the Cornell High Energy Synchrotron Source (CHESS) beamline D1 using a custom apparatus for *in situ* blade coating experiments. Linear translation of the glass blade was powered by a ThorLabs DDSM50 mounted to the side of the stage. Substrates were silicon with a native oxide layer, used without any additional cleaning, diced into strips of both 8 and 16 mm width. N2200 solution in toluene was dispensed into the blade gap remotely via syringe pump, and then, data collection was initiated, followed by blade coating. WAXS collection time was 0.2 s while UV–vis collection time was 0.1 s, and data collection was run for at least 90 s. WAXS patterns were collected by a Pilatus Dectris 300k CCD (487 \times 619 pixels, 172 μm \times 172 μm pixel size) area detector at a beam energy of 12.8 keV in an ambient air environment with 0.2 s exposure time and an angle of incidence of 0.12°. Sample–detector distance was approximately 180 mm from the sample center, and calibration was performed with a silver behenate standard. UV–vis spectra were generated by a combined deuterium:quartz–tungsten–halogen source, which was passed through a Glan–Taylor polarizing beam splitter and sent to two separate spectrometers (Ocean Optics) for parallel and perpendicular channels. Calibration, data reduction, and analysis were performed in Jupyter Notebooks with a Python 3.6 Anaconda environment including the Numpy, Pandas, Matplotlib, pyFAI, and pygix libraries.

■ ASSOCIATED CONTENT

Supporting Information

The Supporting Information is available free of charge on the ACS Publications website at DOI: 10.1021/acs.chemmater.9b00888.

Raw data and detailed analysis procedure for SE, transistor data and analysis with comparison to literature results, additional AFM data and analysis, full in-plane pole figures for rotational GIWAXS, tabulated NEXAFS results, and additional *in situ* data (PDF)

Real-time video of the raw X-ray and UV-vis data (MPG)

■ AUTHOR INFORMATION

Corresponding Author

*E-mail: dean.delongchamp@nist.gov.

ORCID

Nils E. Persson: 0000-0003-0750-5880

Lee J. Richter: 0000-0002-9433-3724

Notes

The authors declare no competing financial interest.

■ ACKNOWLEDGMENTS

N.E.P. gratefully acknowledges financial support from the National Research Council Research Associateship Program and the Materials Genome Initiative. S.E. acknowledges support from the U.S. Department of Commerce, National Institute of Standards and Technology under the financial assistance Award 70NANB17H305. The authors acknowledge Dr. Eliot Gann for his instrumental assistance in NEXAFS data collection and analysis. The authors acknowledge Dr. Detlef Smilgies for his assistance with *in situ* coating experiments at CHESS and Dr. Masa Fukuto and Dr. Ruipeng Li for development of the rotational GIWAXS stage at NSLS-II. Beamline D1 at the Cornell High Energy Synchrotron Source (CHESS) is supported by the National Science Foundation under Award DMR-1332208. Beamline 11BM-CMS is at the National Synchrotron Light Source II, a U.S. Department of Energy (DOE) Office of Science User Facility operated for the DOE Office of Science by Brookhaven National Laboratory under Contract DE-SC0012704. Any mention of commercial products within this paper is for information only; it does not imply recommendation or endorsement by NIST

■ REFERENCES

- (1) Siringhaus, H. 25th Anniversary Article: Organic Field-Effect Transistors: The Path Beyond Amorphous Silicon. *Adv. Mater.* **2014**, *26*, 1319–1335.
- (2) Schwartz, G.; Tee, B. C.-K.; Mei, J.; Appleton, A. L.; Kim, D. H.; Wang, H.; Bao, Z. Flexible Polymer Transistors with High Pressure Sensitivity for Application in Electronic Skin and Health Monitoring. *Nat. Commun.* **2013**, *4*, 1859.
- (3) Knopfmacher, O.; Hammock, M. L.; Appleton, A. L.; Schwartz, G.; Mei, J.; Lei, T.; Pei, J.; Bao, Z. Highly Stable Organic Polymer Field-Effect Transistor Sensor for Selective Detection in the Marine Environment. *Nat. Commun.* **2014**, *5*, 2954.
- (4) Mandal, S.; Dell'Erba, G.; Luzio, A.; Bucella, S. G.; Perinot, A.; Calloni, A.; Berti, G.; Bussetti, G.; Duò, L.; Facchetti, A.; Noh, Y.; Caironi, M. Fully-Printed, All-Polymer, Bendable and Highly Transparent Complementary Logic Circuits. *Org. Electron.* **2015**, *20*, 132–141.
- (5) Facchetti, A. Made to Order. *Nat. Mater.* **2013**, *12*, 598–600.
- (6) Qu, G.; Kwok, J. J.; Diao, Y. Flow-Directed Crystallization for Printed Electronics. *Acc. Chem. Res.* **2016**, *49*, 2756–2764.

(7) Mei, J.; Diao, Y.; Appleton, A. L.; Fang, L.; Bao, Z. Integrated Materials Design of Organic Semiconductors for Field-Effect Transistors. *J. Am. Chem. Soc.* **2013**, *135*, 6724–6746.

(8) Diao, Y.; Shaw, L.; Mannsfeld, S. C. B. Morphology Control Strategies for Solution-Processed Organic Semiconductor Thin Films. *Energy Environ. Sci.* **2014**, *7*, 2145–2159.

(9) Gu, X.; Shaw, L.; Gu, K.; Toney, M. F.; Bao, Z. The Meniscus-Guided Deposition of Semiconducting Polymers. *Nat. Commun.* **2018**, *9*, 534.

(10) Persson, N. E.; Chu, P.-H.; McBride, M.; Grover, M.; Reichmanis, E. Nucleation, Growth, and Alignment of Poly(3-Hexylthiophene) Nanofibers for High-Performance OFETs. *Acc. Chem. Res.* **2017**, *50*, 932–942.

(11) O'Connor, B.; Kline, R. J.; Conrad, B. R.; Richter, L. J.; Gundlach, D.; Toney, M. F.; DeLongchamp, D. M. Anisotropic Structure and Charge Transport in Highly Strain-Aligned Regioregular Poly(3-Hexylthiophene). *Adv. Funct. Mater.* **2011**, *21*, 3697–3705.

(12) Jimison, L. H.; Toney, M. F.; McCulloch, I.; Heeney, M.; Salleo, A. Charge-Transport Anisotropy Due to Grain Boundaries in Directionally Crystallized Thin Films of Regioregular Poly(3-Hexylthiophene). *Adv. Mater.* **2009**, *21*, 1568–1572.

(13) Luzio, A.; Criante, L.; D'Innocenzo, V.; Caironi, M. Control of Charge Transport in a Semiconducting Copolymer by Solvent-Induced Long-Range Order. *Sci. Rep.* **2013**, *3*, 1–6.

(14) Nahid, M. M.; Welford, A.; Gann, E.; Thomsen, L.; Sharma, K. P.; McNeill, C. R. Nature and Extent of Solution Aggregation Determines the Performance of P(NDI2OD-T2) Thin-Film Transistors. *Adv. Electron. Mater.* **2018**, *4*, 1700559.

(15) Bucella, S. G.; Luzio, A.; Gann, E.; Thomsen, L.; McNeill, C. R.; Pace, G.; Perinot, A.; Chen, Z.; Facchetti, A.; Caironi, M. Macroscopic and High-Throughput Printing of Aligned Nanostructured Polymer Semiconductors for MHz Large-Area Electronics. *Nat. Commun.* **2015**, *6*, 8394.

(16) Wang, G.; Huang, W.; Eastham, N. D.; Fabiano, S.; Manley, E. F.; Zeng, L.; Wang, B.; Zhang, X.; Chen, Z.; Li, R.; Chang, R. P. H.; Chen, L. X.; Bedzyk, M. J.; Melkonyan, F. S.; Facchetti, A.; Marks, T. J. Aggregation Control in Natural Brush-Printed Conjugated Polymer Films and Implications for Enhancing Charge Transport. *Proc. Natl. Acad. Sci. U. S. A.* **2017**, *114*, E10066–E10073.

(17) Wu, D.; Kaplan, M.; Ro, H. W.; Engmann, S.; Fischer, D. A.; DeLongchamp, D. M.; Richter, L. J.; Gann, E.; Thomsen, L.; McNeill, C. R.; Zhang, X. Blade Coating Aligned, High-Performance, Semiconducting-Polymer Transistors. *Chem. Mater.* **2018**, *30*, 1924–1936.

(18) Shaw, L.; Hayoz, P.; Diao, Y.; Reinspach, J. A.; To, J. W. F.; Toney, M. F.; Weitz, R. T.; Bao, Z. Direct Uniaxial Alignment of a Donor–Acceptor Semiconducting Polymer Using Single-Step Solution Shearing. *ACS Appl. Mater. Interfaces* **2016**, *8*, 9285–9296.

(19) Patel, B. B.; Diao, Y. Multiscale Assembly of Solution-Processed Organic Electronics: The Critical Roles of Confinement, Fluid Flow, and Interfaces. *Nanotechnology* **2018**, *29*, 044004.

(20) Chu, P.-H.; Kleinhenz, N.; Persson, N.; McBride, M.; Hernandez, J. L.; Fu, B.; Zhang, G.; Reichmanis, E. Toward Precision Control of Nanofiber Orientation in Conjugated Polymer Thin Films: Impact on Charge Transport. *Chem. Mater.* **2016**, *28*, 9099–9109.

(21) Persson, N. E.; Rafshoon, J.; Naghshpour, K.; Fast, T.; Chu, P.-H.; McBride, M.; Risteen, B.; Grover, M.; Reichmanis, E. High-Throughput Image Analysis of Fibrillar Materials: A Case Study on Polymer Nanofiber Packing, Alignment, and Defects in Organic Field Effect Transistors. *ACS Appl. Mater. Interfaces* **2017**, *9*, 36090–36102.

(22) Qu, G.; Zhao, X.; Newbloom, G. M.; Zhang, F.; Mohammadi, E.; Strzalka, J. W.; Pozzo, L. D.; Mei, J.; Diao, Y. Understanding Interfacial Alignment in Solution Coated Conjugated Polymer Thin Films. *ACS Appl. Mater. Interfaces* **2017**, *9*, 27863–27874.

(23) Shaw, L.; Yan, H.; Gu, X.; Hayoz, P.; Weitz, R. T.; Kaelblein, D.; Toney, M. F.; Bao, Z. Microstructural Evolution of the Thin Films of a Donor–Acceptor Semiconducting Polymer Deposited by Meniscus-Guided Coating. *Macromolecules* **2018**, *51*, 4325–4340.

(24) Trefz, D.; Gross, Y. M.; Dingler, C.; Tkachov, R.; Hamidi-Sakr, A.; Kiriy, A.; McNeill, C. R.; Brinkmann, M.; Ludwigs, S. Tuning

Oriental Order of Highly Aggregating P(NDI2OD-T 2) by Solvent Vapor Annealing and Blade Coating. *Macromolecules* **2019**, *52*, 43–54.

(25) DeLongchamp, D. M.; Kline, R. J.; Jung, Y.; Germack, D. S.; Lin, E. K.; Moad, A. J.; Richter, L. J.; Toney, M. F.; Heeney, M.; McCulloch, I. Controlling the Orientation of Terraced Nanoscale “Ribbons” of a Poly(Thiophene) Semiconductor. *ACS Nano* **2009**, *3*, 780–787.

(26) Gemünden, P.; Poelking, C.; Kremer, K.; Andrienko, D.; Daoulas, K. C. Nematic Ordering, Conjugation, and Density of States of Soluble Polymeric Semiconductors. *Macromolecules* **2013**, *46*, 5762–5774.

(27) Delongchamp, D. M.; Kline, R. J.; Fischer, D. A.; Richter, L. J.; Toney, M. F. Molecular Characterization of Organic Electronic Films. *Adv. Mater.* **2011**, *23*, 319–337.

(28) Clark, J.; Silva, C.; Friend, R. H.; Spano, F. C. Role of Intermolecular Coupling in the Photophysics of Disordered Organic Semiconductors: Aggregate Emission in Regioregular Polythiophene. *Phys. Rev. Lett.* **2007**, *98*, 206406.

(29) Rivnay, J.; Mannsfeld, S. C. B.; Miller, C. E.; Salleo, A.; Toney, M. F. Quantitative Determination of Organic Semiconductor Microstructure from the Molecular to Device Scale. *Chem. Rev.* **2012**, *112*, 5488–5519.

(30) Wirix, M. J. M.; Bomans, P. H. H.; Friedrich, H.; Sommerdijk, N. A. J. M.; de With, G. Three-Dimensional Structure of P3HT Assemblies in Organic Solvents Revealed by Cryo-TEM. *Nano Lett.* **2014**, *14*, 2033–2038.

(31) Kleinhenz, N.; Persson, N.; Xue, Z.; Chu, P. H.; Wang, G.; Yuan, Z.; McBride, M. A.; Choi, D.; Grover, M. A.; Reichmanis, E. Ordering of Poly(3-Hexylthiophene) in Solutions and Films: Effects of Fiber Length and Grain Boundaries on Anisotropy and Mobility. *Chem. Mater.* **2016**, *28*, 3905–3913.

(32) Brinkmann, M.; Chandezon, F.; Pansu, R. B.; Julien-Rabant, C. Epitaxial Growth of Highly Oriented Fibers of Semiconducting Polymers with a Shish-Kebab-like Superstructure. *Adv. Funct. Mater.* **2009**, *19*, 2759–2766.

(33) Wang, G.; Persson, N.; Chu, P.; Kleinhenz, N.; Fu, B.; Chang, M.; Deb, N.; Mao, Y.; Wang, H.; Grover, M. A.; Reichmanis, E. Microfluidic Crystal Engineering of π -Conjugated Polymers. *ACS Nano* **2015**, *9*, 8220–8230.

(34) Lim, J. A.; Liu, F.; Ferdous, S.; Muthukumar, M.; Briseno, A. L. Polymer Semiconductor Crystals. *Mater. Today* **2010**, *13*, 14–24.

(35) Usov, I.; Mezzenga, R. Fiber App: An Open-Source Software for Tracking and Analyzing Polymers, Filaments, Biomacromolecules, and Fibrous Objects. *Macromolecules* **2015**, *48*, 1269–1280.

(36) Nordén, B. Applications of Linear Dichroism Spectroscopy. *Appl. Spectrosc. Rev.* **1978**, *14*, 157–248.

(37) Thulstrup, E. W.; Michl, J. *Elementary Polarization Spectroscopy*; VCH Publishers: United States, 1989.

(38) Simpson, G. J.; Westerbuhr, S. G.; Rowlen, K. L. Molecular Orientation and Angular Distribution Probed by Angle-Resolved Absorbance and Second Harmonic Generation. *Anal. Chem.* **2000**, *72*, 887–898.

(39) Le Berre, M.; Chen, Y.; Baigl, D. From Convective Assembly to Landau-Levich Deposition of Multilayered Phospholipid Films of Controlled Thickness. *Langmuir* **2009**, *25*, 2554–2557.

(40) Landau, L.; Levich, B. Dragging of a Liquid by a Moving Plate. *Acta Physicochim. U.R.S.S.* **1942**, *17*, 42–54.

(41) Derjaguin, B. Thickness of Liquid Layer Adhering to Walls of Vessels on Their Emptying and the Theory of Photo-and Motion-Picture Film Coating. In *CR (Dokl.) Acad. Sci. URSS* **1943**, *39*, 13–16.

(42) Yan, H.; Chen, Z.; Zheng, Y.; Newman, C.; Quinn, J. R.; Dötz, F.; Kastler, M.; Facchetti, A. A High-Mobility Electron-Transporting Polymer for Printed Transistors. *Nature* **2009**, *457*, 679–686.

(43) Bittle, E. G.; Basham, J. I.; Jackson, T. N.; Jurchescu, O. D.; Gundlach, D. J. Mobility Overestimation Due to Gated Contacts in Organic Field-Effect Transistors. *Nat. Commun.* **2016**, *7*, 10908.

(44) Chen, Z.; Zheng, Y.; Yan, H.; Facchetti, A. Naphthalenedi-carboximide- vs Perylenedicarboximide-Based Copolymers. Synthesis

and Semiconducting Properties in Bottom-Gate N-Channel Organic Transistors. *J. Am. Chem. Soc.* **2009**, *131*, 8–9.

(45) Salleo, A.; Kline, R. J.; DeLongchamp, D. M.; Chabinyc, M. L. Microstructural Characterization and Charge Transport in Thin Films of Conjugated Polymers. *Adv. Mater.* **2010**, *22*, 3812–3838.

(46) Tessler, N.; Preezant, Y.; Rappaport, N.; Roichman, Y. Charge Transport in Disordered Organic Materials and Its Relevance to Thin-Film Devices: A Tutorial Review. *Adv. Mater.* **2009**, *21*, 2741–2761.

(47) Jalili, R.; Morshed, M.; Ravandi, S. A. H. Fundamental Parameters Affecting Electrospinning of PAN Nanofibers as Uniaxially Aligned Fibers. *J. Appl. Polym. Sci.* **2006**, *101*, 4350–4357.

(48) Persson, N. E.; McBride, M. A.; Grover, M. A.; Reichmanis, E. Automated Analysis of Orientational Order in Images of Fibrillar Materials. *Chem. Mater.* **2017**, *29*, 3–14.

(49) Schuettfort, T.; Watts, B.; Thomsen, L.; Lee, M.; Sirringhaus, H.; McNeill, C. R. Microstructure of Polycrystalline PBTTT Films: Domain Mapping and Structure Formation. *ACS Nano* **2012**, *6*, 1849–1864.

(50) Frenkel, D.; Lekkerkerker, H. N. W.; Stroobants, A. Thermodynamic Stability of a Smectic Phase in a System of Hard Rods. *Nature* **1988**, *332*, 822–823.

(51) Tseng, H. R.; Ying, L.; Hsu, B. B. Y.; Perez, L. A.; Takacs, C. J.; Bazan, G. C.; Heeger, A. J. High Mobility Field Effect Transistors Based on Macroscopically Oriented Regioregular Copolymers. *Nano Lett.* **2012**, *12*, 6353–6357.

(52) Schuettfort, T.; Thomsen, L.; McNeill, C. R. Observation of a Distinct Surface Molecular Orientation in Films of a High Mobility Conjugated Polymer. *J. Am. Chem. Soc.* **2013**, *135*, 1092–1101.

(53) Rivnay, J.; Toney, M. F.; Zheng, Y.; Kauvar, I. V.; Chen, Z.; Wagner, V.; Facchetti, A.; Salleo, A. Unconventional Face-On Texture and Exceptional In-Plane Order of a High Mobility n-Type Polymer. *Adv. Mater.* **2010**, *22*, 4359–4363.

(54) DeLongchamp, D. M.; Kline, R. J.; Lin, E. K.; Fischer, D. A.; Richter, L. J.; Lucas, L. A.; Heeney, M.; McCulloch, I.; Northrup, J. E. High Carrier Mobility Polythiophene Thin Films: Structure Determination by Experiment and Theory. *Adv. Mater.* **2007**, *19*, 833–837.

(55) Sirringhaus, H.; Wilson, R. J.; Friend, R. H.; Inbasekaran, M.; Wu, W.; Woo, E. P.; Grell, M.; Bradley, D. D. C. Mobility Enhancement in Conjugated Polymer Field-Effect Transistors through Chain Alignment in a Liquid-Crystalline Phase. *Appl. Phys. Lett.* **2000**, *77*, 406–408.

(56) Avrami, M. Kinetics of Phase Change. II Transformation-Time Relations for Random Distribution of Nuclei. *J. Chem. Phys.* **1940**, *8*, 212–224.

(57) Stafford, C. M.; Roskov, K. E.; Epps, T. H.; Fasolka, M. J. Generating Thickness Gradients of Thin Polymer Films via Flow Coating. *Rev. Sci. Instrum.* **2006**, *77*, 023908.

(58) Kieffer, J.; Wright, J. P. PyFAI: A Python Library for High Performance Azimuthal Integration on GPU. *Powder Diffr.* **2013**, *28*, S339–S350.